Research Square

Preprints are preliminary reports that have not undergone peer review.
They should not be considered conclusive, used to inform clinical practice,
or referenced by the media as validated information.

Spatiotemporal evolution of mining-induced surface deformation and fissures from InSAR, UAV photogrammetry, and microseismic monitoring

Jiangtao Qiu

qiujiangtao@smac.ac.cn

The Second Monitoring and Application Center, China Earthquake Administration

Xinxin Yin

Earthquake Administration of Gansu Province

Lingyun Ji

The Second Monitoring and Application Center, China Earthquake Administration

Liangyu Zhu

The Second Monitoring and Application Center, China Earthquake Administration

Hongbin Cheng

The Second Monitoring and Application Center, China Earthquake Administration

Zongpan Bian

The Second Monitoring and Application Center, China Earthquake Administration

Haibo Wang

State Key Laboratory of Cryospheric Science and Frozen Soil Engineering, Northwest Institute of Eco-Environment and Resources, Chinese Academy of Sciences

Article

Keywords: InSAR, mining-induced deformation, surface fissures, UAV photogrammetry, microseismicity, time-series analysis

Posted Date: November 24th, 2026

DOI: https://doi.org/10.21203/rs.3.rs-11543930/v1

License: This work is licensed under a Creative Commons Attribution 4.0 International License.
Read Full License

Additional Declarations: No competing interests reported.

Abstract

Mining-induced deformation is spatially extensive, whereas fissures are localized and microseismicity is recorded at event scale. We integrated 47 ascending Sentinel-1A acquisitions (January 2024–March 2026), UAV photogrammetry from 3,629 images, and 6,684 microseismic events (1 September–7 December 2025) from a longwall mining area in Zhengning, northwestern China. InSAR revealed three stages: deformation above previously mined panels, emergence of separate subsidence centres over adjacent panels, and subsequent expansion and coalescence. Maximum cumulative line-of-sight displacement was approximately − 0.45 m. UAV-mapped fissures preferentially followed high displacement-gradient belts rather than the centres of maximum cumulative displacement. During the 98-day microseismic interval, cross-correlation between a first-differenced, windowed Benioff-strain indicator and an InSAR-derived acceleration indicator peaked at R = 0.47 with an approximately 17-day lag, with the seismic indicator leading. This moderate association is case-specific and does not establish causation or a transferable warning time; the two largest energy-release events lacked coincident Sentinel-1 acquisitions, and the in-sample threshold assessment cannot validate event-scale surface synchrony or operational forecasting. The results illustrate the complementary value of regional deformation mapping, localized fissure observations, and short-window seismic records.

Introduction

Mining-induced subsidence and surface damage are common consequences of underground coal extraction. Time-series satellite observations can reconstruct the spatial extent and temporal evolution of deformation, while ground and close-range surveys reveal localized features such as fissures and collapse structures. Reviews of mining-subsidence monitoring emphasize that InSAR, conventional surveying and UAV photogrammetry offer complementary spatial coverage and resolution, although no single method captures every aspect of the process [1, 2].

Time-series InSAR maps broad deformation patterns and displacement histories, but it measures radar LOS motion rather than subsurface fracturing directly [1, 3]. Velocity and acceleration derived from displacement histories can highlight changes in deformation kinematics, although differentiation amplifies noise and makes the indicators sensitive to temporal sampling and filtering [4]. UAV photogrammetry can resolve localized ground fissures and small-scale surface morphology [5]. Microseismic catalogues provide event times, locations and energy information, but their interpretation depends on network configuration and catalogue quality [6, 7]. Multisource comparisons are therefore most informative when each dataset is interpreted at its own spatial and temporal resolution.

The main analytical challenge is to distinguish direct observations from inferences made across datasets with different sampling intervals. This study addresses three questions: (i) how did the InSAR-observed spatial pattern of subsidence change as adjacent longwall panels were mined; (ii) how are UAV-mapped fissures distributed relative to InSAR-derived deformation gradients; and (iii) during the shared observation interval, what statistical lead–lag relationship is observed between a microseismic

activity indicator and surface acceleration? The third question is restricted to the overlap period and does not use the microseismic catalogue to infer earlier deformation stages.

The study area is in the Zhengning mining district of northwestern China, where deep coal workings are overlain by Quaternary loess. This setting provides geographical context, but the available observations do not measure loess mechanical properties or the vertical transfer of deformation through the overburden. Accordingly, the analysis focuses on observed surface deformation, mapped surface features and the temporal association with recorded microseismic activity rather than testing a specific geological mechanism.

We integrate 47 ascending Sentinel-1A acquisitions (Track 84) spanning January 2024 to March 2026, a UAV photogrammetric survey comprising 3,629 images, and a catalogue of 6,684 microseismic events recorded from 1 September to 7 December 2025. The objectives are to describe the InSAR-observed evolution of subsidence, assess the spatial correspondence between UAV-mapped fissures and deformation-gradient patterns, and quantify the statistical lead–lag relationship between microseismic activity and InSAR-derived acceleration during the common observation window. The microseismic record overlaps only the late part of the InSAR-defined Stage III.

The contribution is observational. The InSAR time series documents a transition from one principal deformation basin to separated subsidence centres and then to a coalesced deformation field. UAV mapping indicates a spatial association between surface fissures and high-gradient belts. Cross-correlation of the overlapping records identifies a moderate peak ($R = 0.47$) at an approximately 17-day lag, with the seismic indicator leading the surface-acceleration indicator. This lag is reported as a case-specific statistical relationship, not as proof of causation or a validated warning horizon.

Results

Spatiotemporal evolution of surface deformation

The 47-image SBAS-InSAR time series spanning January 2024 to March 2026 shows a progressive change in the spatial pattern of surface deformation (Fig. 2 and Fig. S2). Maximum cumulative line-of-sight (LOS) displacement is approximately − 0.45 m, and the reported peak deformation rate approaches − 3 mm day^{-1}. These values represent the retrieved LOS component, not full three-dimensional displacement.

Three representative points (P1–P3) within the deforming area were examined together with a reference point (P0) outside the principal mining influence zone (Fig. 2). P1 and P2 are located near the areas associated with the two largest microseismic events on 25 October and 6 December 2025; P3 represents the principal deformation zone above the previously mined 1802–1803 panels.

The unreferred displacement histories show low-amplitude oscillations that occur across multiple monitoring points (Fig. 2g). Referencing the series to P0 reduces a common component and makes the

spatial differences associated with the deforming area clearer (Fig. 2h). InSAR alone does not uniquely separate atmospheric effects, seasonal near-surface signals, and other regional components, so the analysis does not assign a single cause to the common oscillations.

The reference-corrected InSAR series is described in three stages. This is an empirical classification of the surface-deformation record, not a chronology of directly observed subsurface failure.

Stage I (January–August 2024): deformation was concentrated above the previously mined 1802–1803 panels, forming an elongated basin oriented approximately NNW–SSE. Displacement at P3 increased gradually, while P1 and P2 showed comparatively little change.

Stage II (September 2024–May 2025): additional deformation developed above the 2803–2804 panels. Separate subsidence centres became apparent, producing two spatially distinct elongated basins in the mapped field.

Stage III (June 2025–March 2026): deformation over the previously mined panels became less pronounced, while the deformation field above the active 2803–2804 panels expanded. The initially separate basins grew towards one another and ultimately formed a more continuous composite basin. The point histories also became more similar during this stage. The microseismic catalogue covers only the late part of this stage.

Spatial association between deformation gradients and fissures

Cumulative displacement records total retrieved movement, whereas velocity, acceleration and spatial gradients highlight where deformation is changing and concentrating (Fig. 3). In 2024, the highest rates were concentrated above Panels 1802–1803 and later weakened. A second deformation centre appeared above Panels 2803–2804 in late 2024 and migrated northeastward as mining advanced. From April to November 2025, high velocities also occurred between the two mining districts. Profiles A–A' show corresponding changes in velocity, acceleration and displacement-gradient anomalies (Fig. 3j–l). These fields describe surface kinematics and do not directly measure subsurface stress transfer.

UAV photogrammetry mapped a fissure network in the principal deformation area (Fig. 4a–c), with a dominant orientation of approximately 10°–20°. At map scale, fissures preferentially lie along high-gradient zones in the March 2026 InSAR field (Fig. 4e). Gradient values at mapped crack vertices were higher than at random locations (Fig. 4f), supporting a spatial association at the scale of mapped belts, subject to the approximately 3.0 m UAV–InSAR co-registration RMS. Fissures do not follow the centres of maximum cumulative subsidence; they concentrate where the spatial gradient is high. The gradient field therefore provides information on the spatial organization of surface damage that is not conveyed by cumulative displacement alone. InSAR and UAV observations are complementary: InSAR resolves the broader deformation field, whereas UAV imagery resolves localized surface features. Their comparison links fissure locations to gradient patterns but does not establish a deterministic crack-prediction rule.

Spatial and temporal characteristics of microseismicity

The 6,684 microseismic events are spatially clustered, with most located around the advancing Panels 2803–2804 and particularly near the central leading edge of the mining front (Fig. 5a). Fewer events were recorded above the previously mined Panels 1802–1803. Event frequency increased from early September through late October and remained elevated during November, reaching a reported maximum of 142 events day^{-1} on 5 November 2025 (Fig. 5b). These observations describe the supplied catalogue during its 98-day recording interval.

Cumulative Benioff strain provides an energy-weighted summary of event activity (Fig. 5c). The curve includes two pronounced increases associated with the two largest recorded energy-release events, superimposed on a more gradual increase over the catalogue period. The frequency–magnitude relation is reported to have a completeness magnitude of approximately Mc = − 0.85 and a b-value of approximately 3.0. These statistics describe the supplied catalogue; they do not independently establish a particular physical state of the surrounding rock mass.

Temporal association between microseismic activity and surface acceleration

The temporal comparison was restricted to 1 September–7 December 2025, the interval covered by the microseismic catalogue. The main statistic was the cross-correlation between the first-differenced, windowed Benioff-strain indicator and the InSAR-derived surface-acceleration indicator (Fig. 6).

Cross-correlation reaches a maximum of R = 0.47 at a lag of approximately + 17 days, where positive lag denotes the seismic indicator leading the surface-acceleration indicator. This is a moderate statistical association observed within a short common interval. The Sentinel-1 acquisition schedule is irregular and includes a 48-day gap between 19 September and 6 November 2025 (Supplementary Table S1). Daily interpolation of the displacement record does not add independent SAR observations, and the 17-day lag should not be interpreted as a precisely resolved physical delay.

The two largest microseismic energy-release events occurred on 25 October and 6 December 2025, dates without corresponding Sentinel-1 acquisitions. In addition, the 31-day Savitzky–Golay differentiation window smooths the retrieved kinematic series. Consequently, apparent proximity between these event dates and changes in the derived acceleration curve cannot establish a synchronous surface response. The moderate correlation also indicates that the microseismic indicator does not account for all temporal variation in the surface indicator.

Exploratory threshold assessment

The observed lead–lag relationship motivated an exploratory assessment of whether the Benioff-strain indicator could flag high-acceleration intervals. The normalized daily increment of Benioff strain was

compared with a surface-acceleration threshold defined as the 80th percentile of the observation period. The exercise uses only the short common record and is not an independent forecast test.

The selected knee-point solution corresponds to a normalized Benioff-strain threshold of approximately 0.04 and a trailing observation window of 19 days. In the analysed interval, it yielded a probability of detection (POD) of 1.00 and a false-alarm rate (FAR) of approximately 0.63. The perfect in-sample detection rate is accompanied by a substantial false-alarm rate and should not be interpreted as evidence of operational reliability.

The false-alarm rate indicates that many alarms were not followed by a threshold-exceeding surface-acceleration interval within the defined window. Given the short record and the use of the same observations for threshold selection and assessment, the POD and FAR values are descriptive rather than out-of-sample performance estimates.

The microseismic indicator is therefore a candidate for further evaluation, not a validated precursor or an operational warning rule. The result is reported as an exploratory assessment of the existing record.

Discussion

The InSAR time series provides the longest temporal record in this study and directly documents three empirical stages: deformation concentrated above previously mined panels, emergence of separate subsidence centres over adjacent panels, and subsequent expansion and coalescence of the deformation field. These patterns are supported by the displacement maps and representative point histories. They describe the evolving surface response but do not, by themselves, resolve the internal state of roof layers, subsurface fractures or stress transfer between mined panels.

The UAV–InSAR comparison adds a local-scale observation to the regional deformation field. Mapped fissures are preferentially associated with high-gradient belts rather than the centres of maximum cumulative LOS displacement. Cumulative displacement and spatial gradient describe different features of the surface field: the former summarizes total retrieved motion, while the latter identifies locations where motion changes sharply across space. Given the reported co-registration RMS of approximately 3.0 m, the result should be interpreted at the scale of mapped belts and features, not as pixel-level correspondence or a deterministic crack-prediction rule.

The microseismic catalogue contributes event-level information only for 1 September–7 December 2025, overlapping the late part of InSAR Stage III. The 6,684 events are concentrated around the advancing Panels 2803–2804, and the energy record is punctuated by two large releases. Previous studies have used microseismic event timing, location and energy to characterize mining-related fracture activity and strata movement [6, 7, 14]. Here, these statistics describe the supplied catalogue; they do not independently identify a specific physical state of the rock mass.

For the overlap interval, cross-correlation peaks at R = 0.47 at approximately + 17 days, with the seismic indicator leading the surface-acceleration indicator. Sensitivity tests using 7-, 14-, 21- and 28-day Benioff accumulation windows place the peak at the same lag, with R ranging from 0.45 to 0.49 (Supplementary Text S2). This consistency across the tested accumulation windows does not remove uncertainty associated with the 48-day SAR acquisition gap, the 31-day differentiation window, temporal interpolation or autocorrelation in the processed series. The 17-day offset is a case-specific statistical lead–lag estimate, not a measured propagation time or a fixed warning horizon.

The two largest energy-release events occurred on 25 October and 6 December 2025, but no Sentinel-1 acquisitions were available on either date. Any apparent alignment between these event dates and the filtered acceleration curve therefore relies on an interpolated indicator rather than a surface observation acquired at the event time. The available record cannot establish near-synchronous surface responses or show that lower-energy activity caused or uniquely predicted the larger events.

The exploratory threshold assessment further illustrates the distinction between an in-sample indicator test and an operational forecast. The selected threshold achieved POD = 1.00 but FAR ≈ 0.63 on the same short record used for tuning. With a high false-alarm rate and no independent test interval, these values are descriptive only. They do not demonstrate predictive performance beyond the analysed observation window.

Together, the datasets provide complementary but non-equivalent evidence: InSAR resolves regional deformation over more than two years, UAV photogrammetry maps localized surface fissures, and microseismic monitoring characterizes underground activity during a 98-day overlap. The study documents the spatial evolution of the surface-deformation field, the association between fissures and high-gradient belts, and a moderate short-window statistical relationship between microseismic activity and surface acceleration. It does not establish a complete subsurface-to-surface causal sequence. Interpretation is limited by irregular SAR sampling, the short microseismic record, uncertainty in acceleration derived from filtered and interpolated displacement, and the absence of independent forecast validation.

Methods

Study area and mining context

The study area is in Zhengning County, eastern Gansu Province, China, along the southwestern margin of the Ordos Basin (Fig. 1). It lies on the Chinese Loess Plateau at elevations of approximately 920–1,300 m, in a gently undulating tableland dissected by gullies. Quaternary loess locally reaches an average thickness of about 200 m [8]. These geographic details describe the site; the study does not independently quantify the effect of loess properties on the observed deformation.

The site description is used to locate the monitoring observations. No site-specific geomechanical parameters were measured or incorporated into a physical model.

Coal extraction targets the No. 8 seam of the Middle Jurassic Yan'an Formation at an approximate depth of 600–1,000 m, using fully mechanized longwall top-coal caving. The immediate roof is described in the available mine-geology information as predominantly sandstone. These details provide operational context and are not used to derive a quantitative mechanical model.

Two groups of longwall panels are relevant to the observations. Panels 1802–1803 had been mined before the InSAR observation period, whereas neighbouring Panels 2803–2804 were mined during the period considered. The sequence allows the surface-deformation record above previously mined and active panels to be compared within one satellite time series.

Monitoring datasets

The analysis used four datasets: Sentinel-1 SAR observations for surface deformation, a digital elevation model (DEM) for topographic-phase removal, UAV imagery for high-resolution surface mapping, and a microseismic catalogue for event-based characterization of underground activity.

A total of 47 ascending Sentinel-1A acquisitions (Track 84) from January 2024 to March 2026 were used. The images were acquired in Interferometric Wide Swath mode with VV polarization and an incidence angle of approximately 38.6°. Acquisition dates were not uniformly spaced.

The 30-m Copernicus DEM was used to remove the topographic phase contribution during differential interferogram formation.

A low-altitude UAV survey covered the principal deformation and fissure zone. A total of 3,629 overlapping visible-light photographs were acquired, with a reported ground sampling distance of approximately 2.2 cm.

The microseismic catalogue contains 6,684 events recorded from 1 September to 7 December 2025. It provides event times, locations and energy information for summarizing event distribution, frequency and energy release. Because the record spans 98 days and overlaps only the late part of the InSAR chronology, it was used only for analysis of the common observation window. Network configuration and event-location uncertainty were not available for independent assessment.

These sources have different spatial and temporal supports: the InSAR series spans more than two years, the UAV survey resolves local surface features over a limited footprint, and the microseismic catalogue covers a 98-day interval. Their comparison was designed to retain these differences rather than treating the datasets as continuous, directly interchangeable observations.

Overview of the analytical workflow

The workflow comprised four steps: (1) retrieve the Sentinel-1 displacement time series using SBAS-InSAR; (2) derive filtered velocity, acceleration and spatial-gradient indicators from the displacement field; (3) map surface fissures from the UAV photogrammetric products and compare their locations with InSAR-derived gradients; and (4) compare the microseismic activity indicator with the surface-

acceleration indicator during the shared observation interval, followed by an exploratory threshold assessment.

SBAS-InSAR processing

Surface deformation was retrieved using the Small Baseline Subset InSAR (SBAS-InSAR) technique, which reconstructs deformation histories from multiple interferograms with short temporal and spatial baselines [3].

Precise orbit ephemerides were applied and the acquisitions were co-registered to a common master image. Differential interferograms were formed using maximum temporal and perpendicular baseline thresholds of 90 days and 90 m, respectively, producing a connected network of 126 interferometric pairs. Goldstein adaptive filtering was applied before phase unwrapping with the minimum-cost-flow algorithm [9, 10]. The time-series displacement solution was estimated by singular value decomposition. Residual atmospheric effects were reduced using the reported spatiotemporal Gaussian–Markov filtering strategy.

An 8:2 multilooking strategy was applied, and pixels with temporal coherence below 0.35 were excluded. Because InSAR provides relative LOS displacement, the time series was referenced to stable areas outside the principal mining-influence zone. Subtracting the reference-point displacement reduced common-mode components in the time series; it does not prove that all residual atmospheric or orbital errors were removed.

Kinematic indicators and spatial gradients

Displacement histories were used to derive velocity and acceleration, and spatial gradients were used to characterize how deformation varied across the surface. These indicators complement cumulative displacement but are not direct measurements of subsurface strain or fracture.

Differentiation of discrete InSAR displacement amplifies noise. Acceleration is therefore treated as a scale-dependent indicator derived from filtered displacement, not as a noise-free measurement of physical acceleration. A two-stage Savitzky–Golay (SG) procedure was applied [4, 11]. The sensitivity analysis in Supplementary Text S1 compares 7-, 15-, 31- and 45-day derivative windows and identifies 31 days as a compromise between smoothing and transient retention. This test does not establish absolute accuracy; acceleration patterns and event timing are interpreted cautiously where SAR acquisitions are widely spaced.

First, a five-epoch, second-order SG filter was applied to each coherent-pixel displacement history. The smoothed series was then interpolated to a daily grid, and a 31-day SG filter was used to calculate velocity and acceleration. Daily interpolation regularizes the computational grid but does not create new independent surface observations. The acceleration series is therefore interpreted as a filtered kinematic indicator, and its apparent short-term timing is not treated as having daily observational resolution.

Spatial gradients of displacement and velocity were calculated on the deformation grid using finite-difference operators. Gradient magnitude was used to identify belts where displacement or velocity changes rapidly across short distances. These are kinematic measures of spatial variation, not direct measurements of material strain.

UAV fissure mapping and spatial comparison

UAV photogrammetry was used to map the surface morphology of the principal deformation zone and compare fissure locations with InSAR-derived deformation patterns.

A DJI Matrice 4E UAV acquired 3,629 overlapping photographs. Five GNSS-RTK-surveyed ground control points were used in the photogrammetric project. The reported bundle-adjustment 3-D RMSE is approximately 0.4 mm; this value is not treated as an independent estimate of field-scale georeferencing accuracy. For comparison with InSAR, the orthomosaic was resampled to 0.39 m per pixel; the reported UAV–InSAR co-registration RMS is approximately 3.0 m (Supplementary Fig. S6). Spatial correspondence is therefore interpreted at the scale of mapped belts and features rather than individual pixels.

Fissures, collapse pits, graben-like features and scarps were mapped by visual interpretation of the orthomosaic, local relief and surface discontinuities. Mapped fissure traces were compared with the InSAR displacement-gradient field. This comparison evaluates spatial association; it does not imply that the gradient field alone predicts the timing or occurrence of every fissure.

Microseismic–surface time-series analysis

To characterize the temporal relationship between microseismic activity and surface deformation, an energy-based seismic indicator was compared with the InSAR-derived acceleration indicator during the common observation window.

Cumulative Benioff strain was used as an energy-weighted proxy for microseismic activity and calculated from the recorded seismic energy of individual events [12]:

$$\epsilon_B(t) = \sum_{i=1}^{M(t)} \sqrt{E_i}$$

where E_i is the seismic energy of the i-th event and $M(t)$ denotes the cumulative number of events up to time (t).

The daily 95th percentile of absolute LOS acceleration within the panel outlines was used as the surface indicator. Its temporal association with the first-differenced, windowed Benioff-strain indicator was evaluated using discrete cross-correlation. A positive lag denotes the seismic indicator leading the surface indicator. Cross-correlation quantifies statistical co-variation and relative timing; it does not establish a causal mechanism. The short overlap and potential autocorrelation in both series limit the interpretation of nominal significance.

$$R_{ae}(\Delta t) = \sum_k \left[\epsilon_B(t_k) - \bar{\epsilon}_B\right]\left[a_{max}(t_k + \Delta t) - \bar{a}\right]$$

where Δt represents the time lag between underground damage evolution and surface acceleration.

Because two high-energy events (reported radiated energy of approximately 10^9 J) occurred during the monitoring period, daily energy release alone could be dominated by extreme observations. Benioff strain was therefore accumulated using a 14-day moving window to represent a smoothed temporal pattern of seismic-energy release. Lags from − 30 to + 30 days were examined. Sensitivity tests using 7-, 14-, 21- and 28-day accumulation windows are reported in Supplementary Text S2.

Exploratory threshold assessment

An exploratory threshold assessment examined whether the seismic indicator could identify high-acceleration intervals in the same observation period. The Non-dominated Sorting Genetic Algorithm II (NSGA-II) was used to explore the trade-off between detection and false alarms [13]. This exercise is descriptive and was not designed as a validated operational warning system.

The predictor was the normalized daily increment of cumulative Benioff strain after three-day moving-average smoothing. A high-acceleration interval was defined as a day on which the absolute surface-acceleration indicator exceeded the 80th percentile of the observation period.

An early-warning rule was parameterized by two variables: the normalized Benioff-strain threshold θ and the trailing observation window w. An alarm was triggered whenever the smoothed Benioff-strain increment exceeded θ within the previous (w) days.

Performance was summarized using the probability of detection (POD) and false-alarm rate (FAR). An interval was counted as detected when at least one alarm occurred within the specified look-back window before a high-acceleration interval. Alarms not followed by a high-acceleration interval within that window were counted as false alarms. Because the same short record was used for threshold selection and assessment, the metrics are in-sample descriptions.

NSGA-II generated candidate thresholds representing the trade-off between detection and false alarms. The knee-point solution was selected as a compact summary of this trade-off, not as an operationally recommended threshold. Its performance must be interpreted in light of the short record, the limited number of high-acceleration intervals and the use of the same data for tuning and assessment.

Data availability

Sentinel-1A SAR data are publicly available through the Copernicus Data Space Ecosystem. The microseismic catalogue and mine-panel vectors were supplied by the mine monitoring team and are not publicly hosted with this manuscript; access requests should be directed to the corresponding author and are subject to permission from the data provider. UAV-derived products and processed time series may be requested from the corresponding author, subject to applicable data-access permissions.

Declarations

Competing interests

The authors declare no competing interests.

Author Contribution

All authors have made substantial contributions to this study and have approved the final version of the manuscript.The study was conceived and designed by Jiangtao Qiu and Xinxin Yin. Data processing and analysis were conducted by Jiangtao Qiu, Lingyun Ji and Zongpan Bian , including the time-series InSAR analysis, UAV photogrammetric analysis, and integration of microseismic observations. Liangyu Zhu, Hongbin Cheng and Haibo Wangcontributed to the interpretation of the geological and geohazard processes. The manuscript was initially drafted by Xinxin Yin and critically revised by all authors. All authors have read and approved the final manuscript and agree to be accountable for all aspects of the work.

Acknowledgement

We thank the mine monitoring team for access to the microseismic catalogue and mining-engineering vectors. This study used only open-source scientific-computing tools.

Data Availability

Sentinel-1A SAR data are publicly available through the Copernicus Data Space Ecosystem. The microseismic catalogue and mine-panel vectors were supplied by the mine monitoring team and are not publicly hosted with this manuscript; access requests should be directed to the corresponding author and are subject to permission from the data provider. UAV-derived products and processed time series may be requested from the corresponding author, subject to applicable data-access permissions.

References

1. Cai, Y. et al. A review of monitoring, calculation, and simulation methods for ground subsidence induced by coal mining. *Int. J. Coal Sci. Technol.* **10**, 32. https://doi.org/10.1007/s40789-023-00595-4 (2023).
2. Tang, F. & Yang, Q. Progress and prospects of multi-source remote sensing monitoring technology for coal mining subsidence in mining areas of the western Loess Plateau. *Coal Sci. Technol.* https://doi.org/10.12438/cst.2023-1113 (2023).

3. Berardino, P., Fornaro, G., Lanari, R. & Sansosti, E. A new algorithm for surface deformation monitoring based on small baseline differential SAR interferograms. *IEEE Trans. Geosci. Remote Sens.* **40**, 2375–2383 (2002).
4. Carlà, T. et al. Perspectives on the prediction of catastrophic slope failures from satellite InSAR. *Sci. Rep.* **9**, 14137 (2019).
5. Zhao, Y. et al. Identification of mining induced ground fissures using UAV and infrared thermal imager: temperature variation and fissure evolution. *ISPRS J. Photogramm Remote Sens.* **180**, 45–64. https://doi.org/10.1016/j.isprsjprs.2021.08.005 (2021).
6. Ghosh, G. K. & Sivakumar, C. Application of underground microseismic monitoring for ground failure and secure longwall coal mining operation: a case study in an Indian mine. *J. Appl. Geophys.* **150**, 21–39. https://doi.org/10.1016/j.jappgeo.2018.01.004 (2018).
7. Liu, F., Wang, Y., Kou, M. & Liang, C. Applications of microseismic monitoring technique in coal mines: a state-of-the-art review. *Appl. Sci.* **14**, 1509. https://doi.org/10.3390/app14041509 (2024).
8. Zhao, D. et al. Study on mining subsidence deformation and failure in loess gully region of Ordos. *Coal Sci. Technol.* **50**, 185–195 (2022).
9. Goldstein, R. M. & Werner, C. L. Radar interferogram filtering for geophysical applications. *Geophys. Res. Lett.* **25**, 4035–4038 (1998).
10. Pepe, A. & Lanari, R. On the extension of the minimum cost flow algorithm for phase unwrapping of multitemporal differential SAR interferograms. *IEEE Trans. Geosci. Remote Sens.* **44**, 2374–2383 (2006).
11. Savitzky, A. & Golay, M. J. E. Smoothing and differentiation of data by simplified least squares procedures. *Anal. Chem.* **36**, 1627–1639. https://doi.org/10.1021/ac60214a047 (1964).
12. Benioff, H. Earthquakes and rock creep (Part I: creep characteristics of rocks and the origin of aftershocks). *Bull. Seismol. Soc. Am.* **41**, 31–62. https://doi.org/10.1785/BSSA0410010031 (1951).
13. Deb, K., Pratap, A., Agarwal, S. & Meyarivan, T. A fast and elitist multiobjective genetic algorithm: NSGA-II. *IEEE Trans. Evol. Comput.* **6**, 182–197. https://doi.org/10.1109/4235.996017 (2002).
14. Cheng, G., Ma, T., Tang, C., Liu, H. & Wang, S. A zoning model for coal mining-induced strata movement based on microseismic monitoring. *Int. J. Rock. Mech. Min. Sci.* **94**, 123–138. https://doi.org/10.1016/j.ijrmms.2017.03.001 (2017).
15. Additional information.

Figures

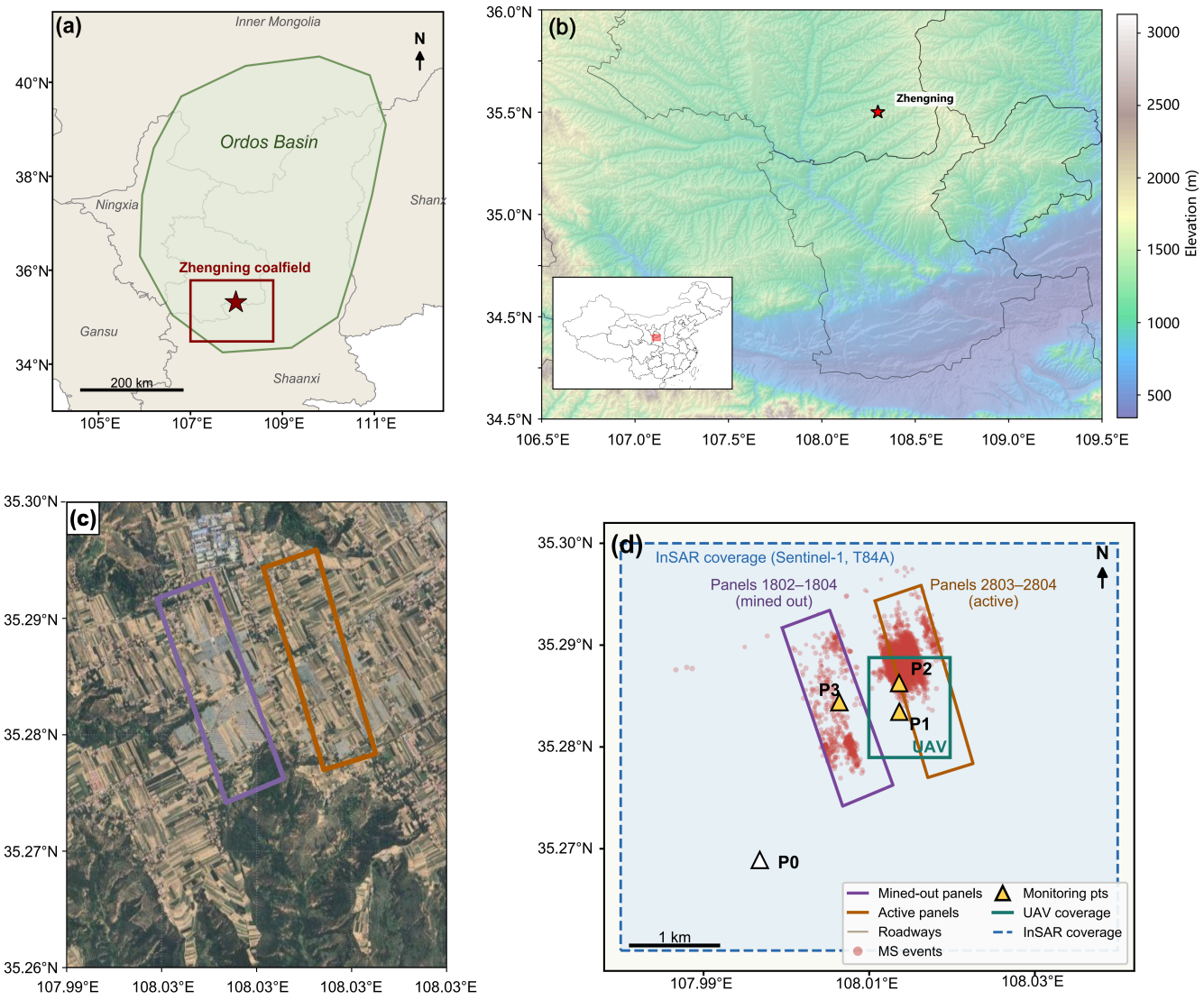

Figure 1

Study area and monitoring configuration in the Zhengning coalfield, Ordos Basin, China.

(a) Location of the Zhengning coalfield on the southwestern margin of the Ordos Basin. (b) Regional topography. (c) Satellite image showing longwall-panel locations. Panels 1802–1803 had been mined before the observation period, whereas Panels 2803–2804 were active during the period considered. (d) Monitoring overview showing Sentinel-1 coverage, the UAV survey area, representative InSAR points (P0–P3), microseismic events and panel boundaries. P0 is the reference point outside the principal mining-influence zone. LOS, line of sight; UAV, unmanned aerial vehicle; DOM, digital orthomosaic; P95, 95th percentile; POD, probability of detection; FAR, false-alarm rate; NSGA-II, non-dominated sorting genetic algorithm II.

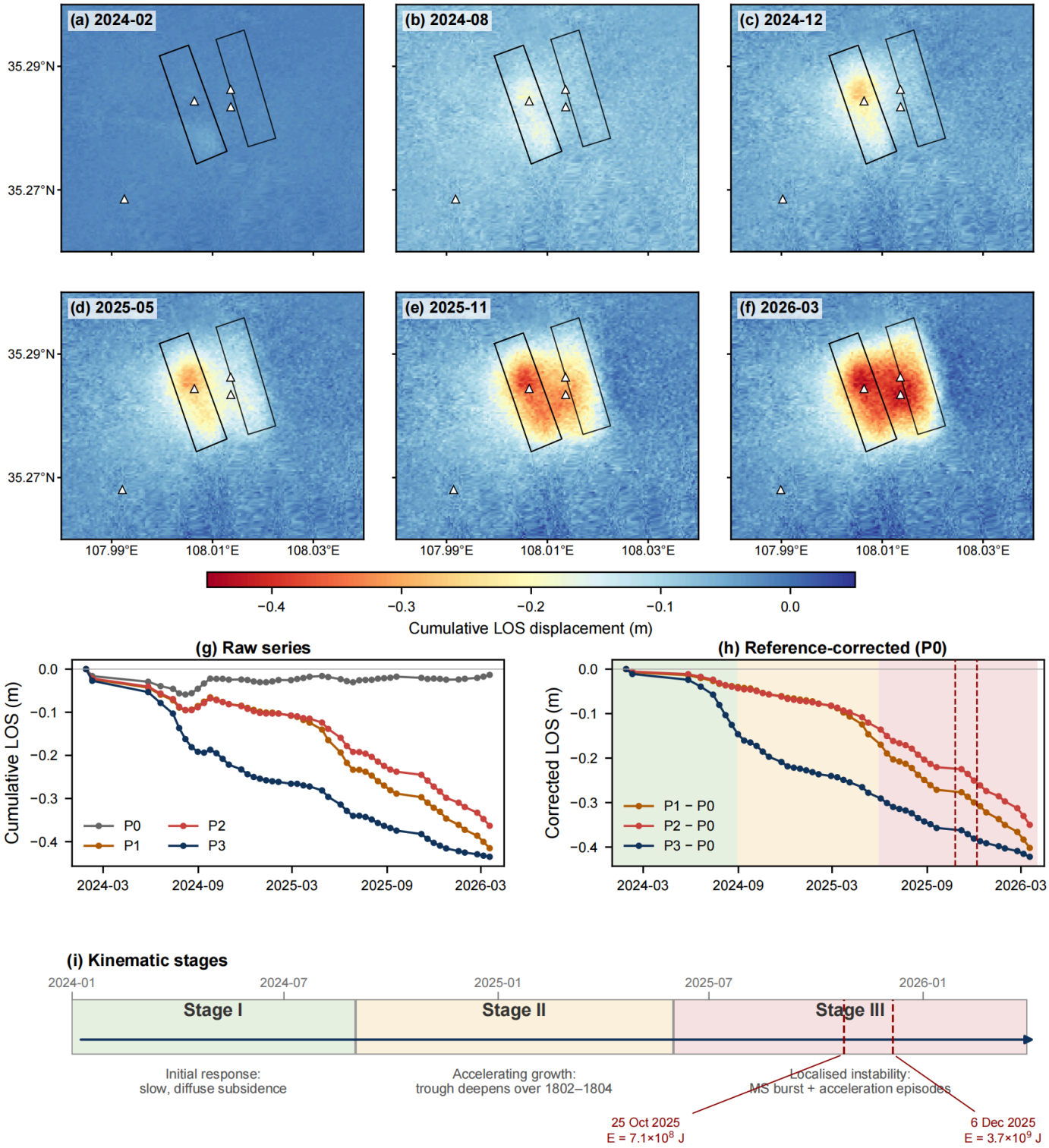

Figure 2

Progressive surface deformation revealed by InSAR during longwall mining.

(a–f) Cumulative LOS displacement maps from February 2024 to March 2026 showing the changing spatial pattern of subsidence. (g) Original LOS displacement histories at P0–P3. (h) Histories referenced to P0. Background shading denotes the three empirical InSAR stages: Stage I, deformation above

previously mined panels; Stage II, emergence of separate deformation centres; and Stage III, expansion and interaction of the deformation basins. Vertical dashed lines mark the two high-energy microseismic event dates; they do not imply that Sentinel-1 acquisitions were available on those dates.

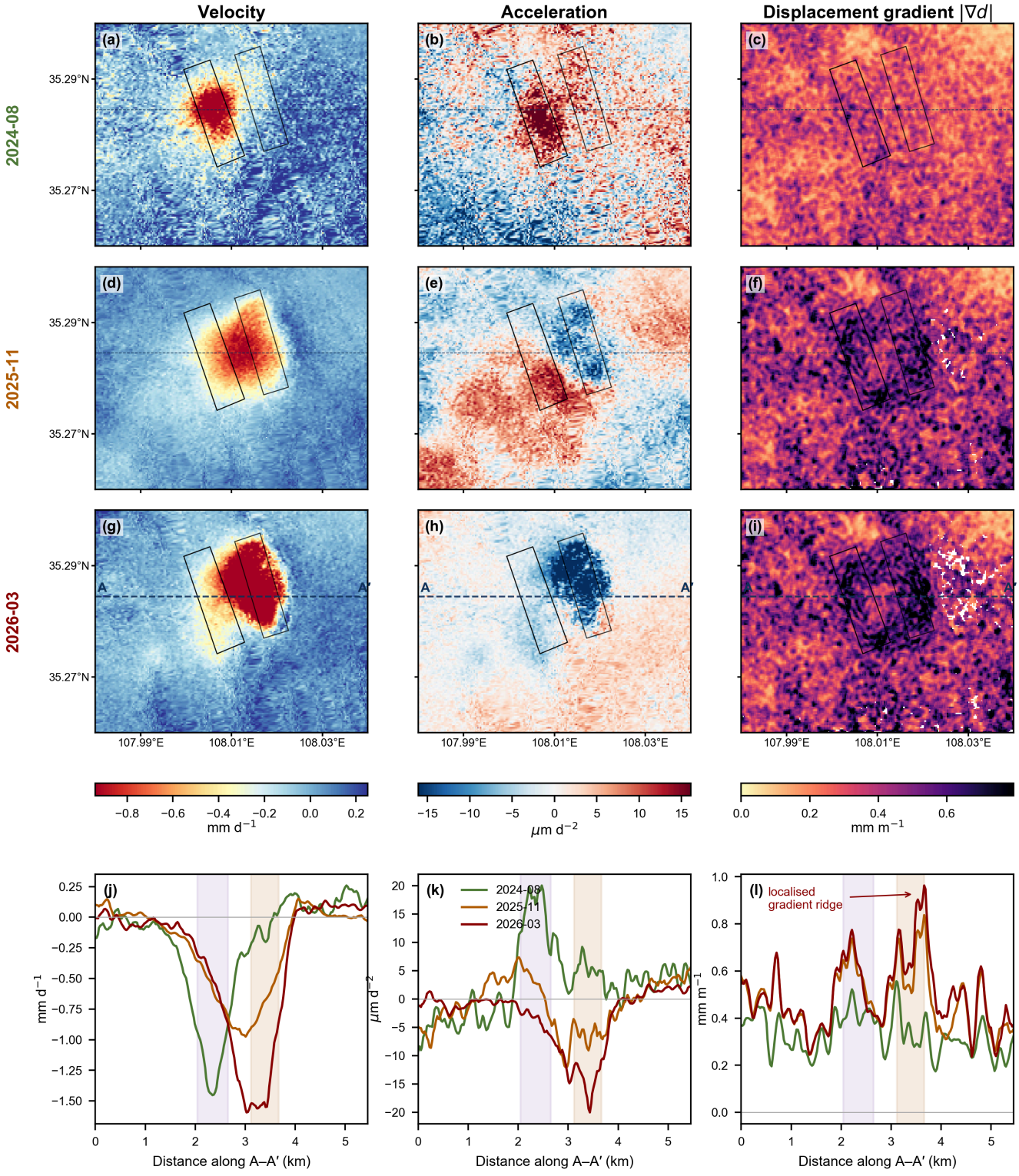

Figure 3

Spatiotemporal evolution of deformation velocity, acceleration and displacement gradient.

(a–i) Surface velocity, acceleration and displacement-gradient magnitude (|∇d|) for August 2024, November 2025 and March 2026. The dashed line A–A' marks the profile location. (j–l) Profiles of velocity, acceleration and displacement-gradient magnitude along A–A'. Acceleration should be interpreted in light of the filtering and sampling limitations described in Methods.

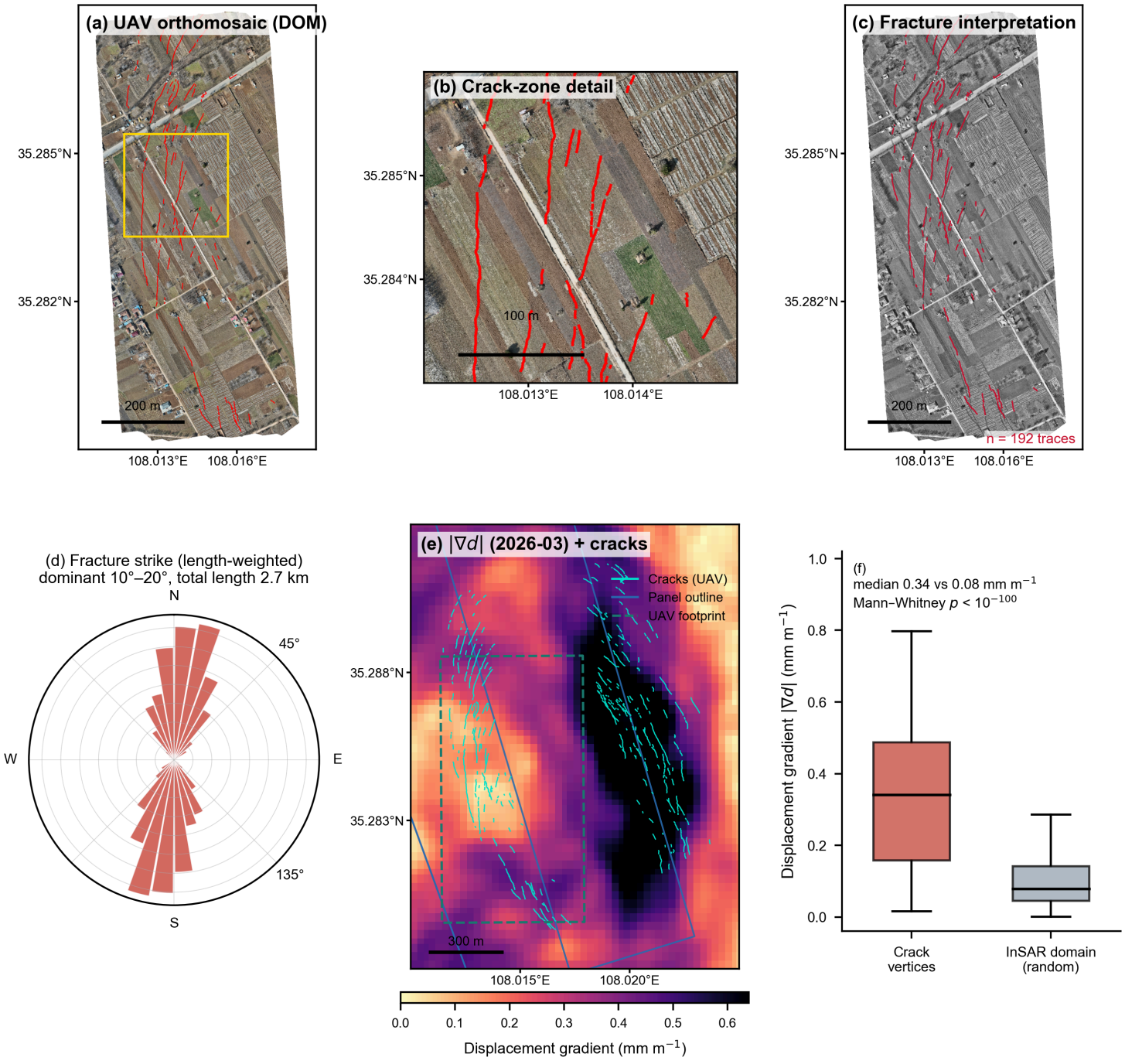

Figure 4

UAV observations of surface fissures and their spatial correspondence with InSAR-derived deformation gradients.

(a) UAV orthomosaic showing mapped surface fissures. (b) Enlarged view of the main fissure zone. (c) Interpreted fissure traces. (d) Length-weighted rose diagram showing the reported dominant orientation of approximately 10°–20°. (e) Fissure traces overlaid on the March 2026 InSAR displacement-gradient field. (f) Comparison of gradient values at mapped crack vertices and random sample locations. The comparison indicates a spatial association with high-gradient zones; it does not demonstrate predictive performance.

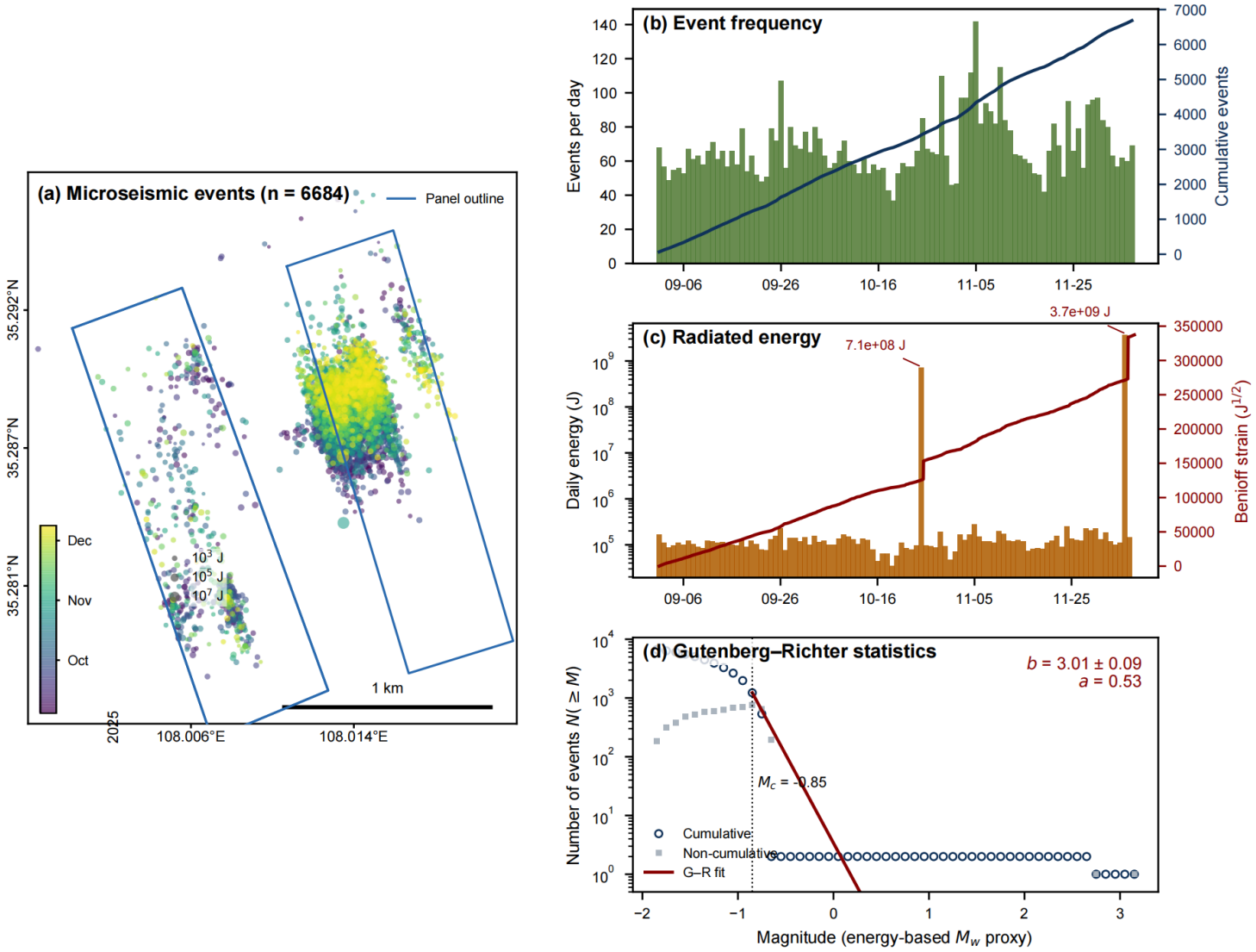

Figure 5

Characteristics of underground microseismic activity during the monitoring period.

(a) (a) Spatial distribution of 6,684 microseismic events, coloured by occurrence time and scaled by radiated energy. (b) Daily and cumulative event frequencies. (c) Daily radiated energy and cumulative Benioff strain, showing two major energy-release episodes. (d) Gutenberg–Richter frequency–magnitude relationship derived from the energy-equivalent magnitude; the reported completeness magnitude is Mc ≈ −0.85 and the b-value is approximately 3.0.

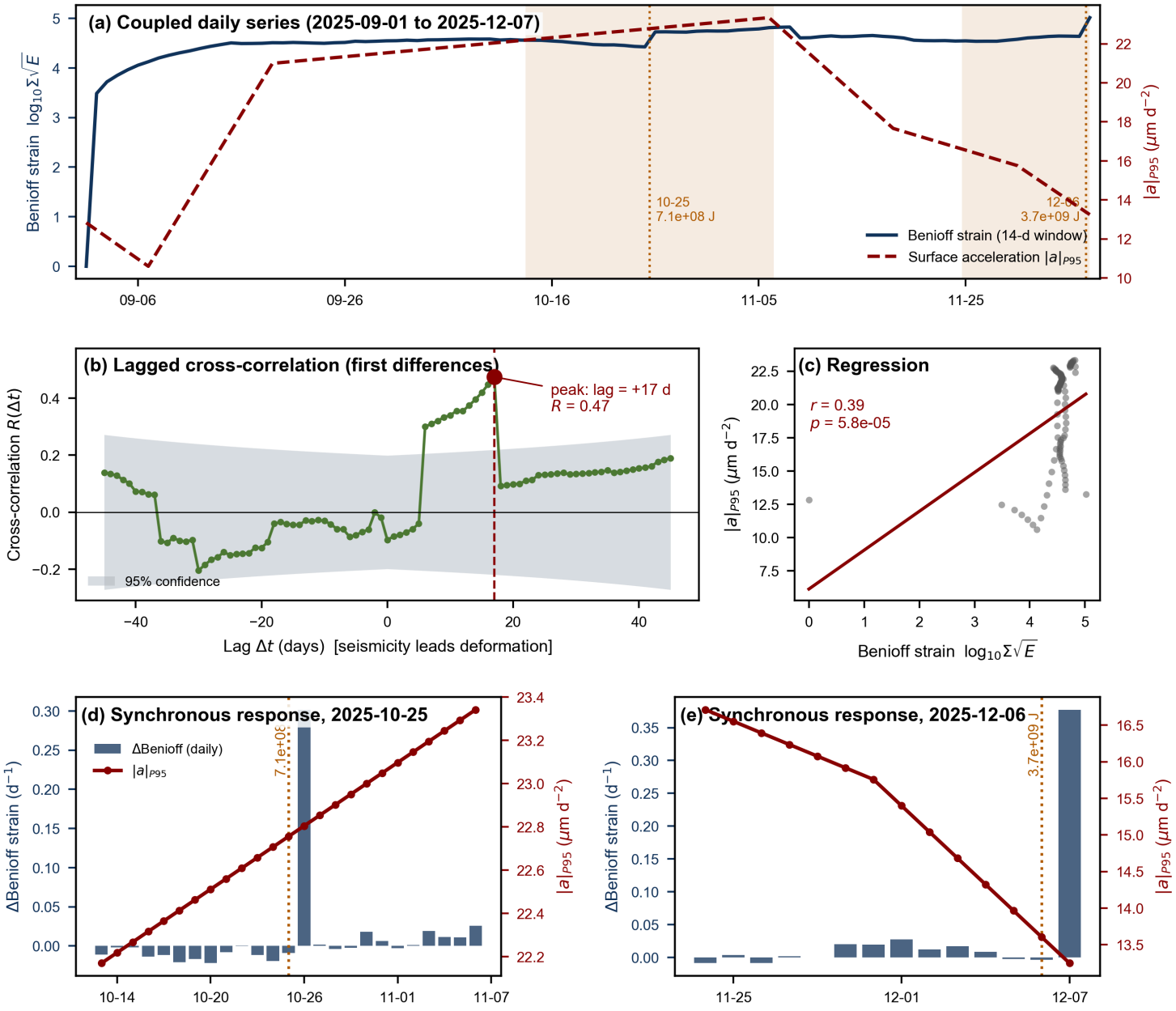

Figure 6

Temporal association between microseismic activity and the InSAR-derived surface-acceleration indicator.

(a) Cumulative Benioff strain and the 95th-percentile absolute LOS acceleration (|a|P95) during the common observation window. (b) Cross-correlation between the first-differenced Benioff-strain indicator and surface acceleration; positive lag means the seismic indicator leads. The peak is approximately R = 0.47 at +17 days. (c) Relationship between the two indicators after lag adjustment. (d–e) Event-centred views of the derived acceleration series around the two largest energy-release events. No Sentinel-1 acquisition occurred on either event date, and the filtered/interpolated series therefore cannot resolve instantaneous synchrony.

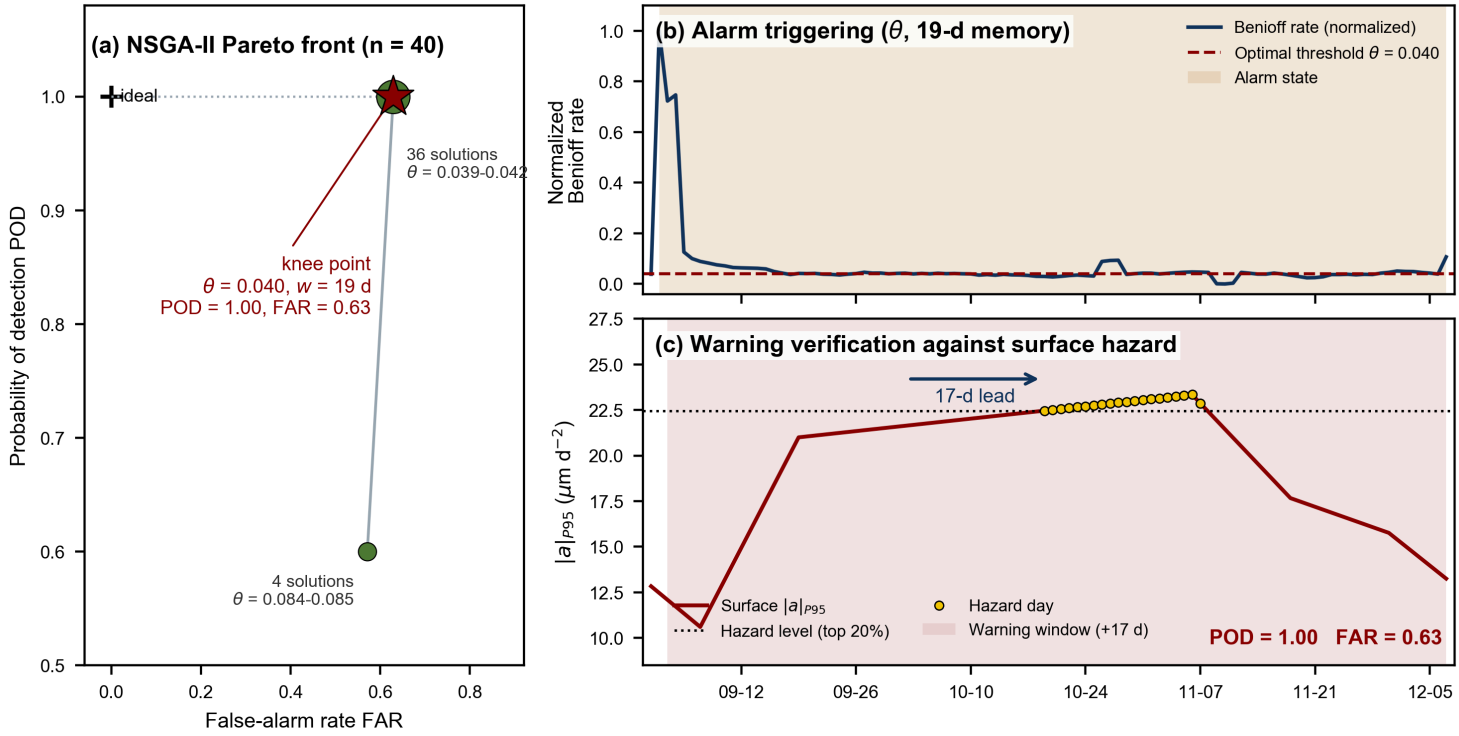

Figure 7

Exploratory threshold assessment of the microseismic activity indicator.

(a) Pareto-optimal solutions from the NSGA-II trade-off analysis. The selected knee-point solution has a normalized alarm threshold of θ = 0.040 and a 19-day look-back window. (b) Alarm states generated by this parameter pair. (c) Comparison between alarm periods and high-acceleration intervals in the same record. The in-sample metrics are POD = 1.00 and FAR ≈ 0.63; they do not represent independent forecast validation.

Supplementary Files

This is a list of supplementary files associated with this preprint. Click to download.

- SRSupplementaryInformation.docx